Convolutional Neural Network-Enabled Optical Fiber SPR Sensors for RI Prediction

Xiao-xiao Liao, Hong Yang, Qiang Wu, Juan Liu, Yingying Hu, Yue Zhang, Wei-qing Liu, Yue Fu, Andrew R Pike, and Bin Liu

***Abstract*—The advancement of artificial intelligence technology has led to the widespread adoption of deep learning techniques within spectral analysis over recent years. In this study, we introduce an advanced demodulation approach utilizing a one-dimensional convolutional neural network (1D-CNN) for feature extraction and the analysis of spectral signals from surface plasmon resonance (SPR) fiber refractive index sensors featuring a multimode-no-core-multimode (MNM) structure while simultaneously forecasting changes in refractive index due to environmental factors. Through segmentation-based predictive training on spectral signals, our approach achieves an average prediction accuracy exceeding 98%, even at low resolutions. Experimental findings demonstrate superior demodulation performance using our intelligent demodulation technique based on 1D-CNN compared to conventional methods. Furthermore, our method is adaptable across diverse and intricate structures enabling observation of parameter correlations spanning their entire range; thereby enhancing measurement capabilities within SPR sensing systems with significant potential applications.**

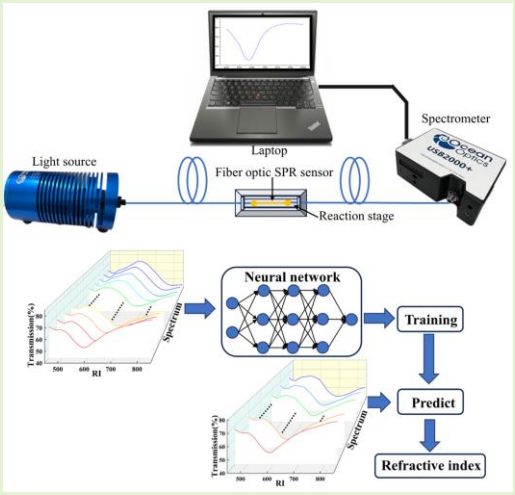

***Index Terms*— Surface plasmonic resonance, refractive index sensing, multimode-core-less multimode structure, one-dimensional convolutional neural network.**

I. INTRODUCTION

Due to its exceptional performance in refractive index (RI) sensing, surface plasmon resonance (SPR) has found extensive applications in various fields including biosensors [1], environmental monitoring [2], food safety [3], and pharmaceutical development [4]. Fiber optic SPR sensors were initially proposed by R. C. Jorgensen in 1993 and have since garnered increasing attention and research efforts over the past few decades [5]. In comparison with traditional prism SPR sensors, optical fiber SPR sensors offer advantages such as compact size, cost-effectiveness, flexibility, and robust remote sensing capabilities. For optical fiber SPR sensors, common types include D-type optical fiber SPR sensors [6], heterocore optical fiber SPR sensors [7], multi-mode optical fiber SPR sensors [8], and photonic crystal fiber SPR sensors [9]. Among various fiber optic interferometers, the MNM (multimode-coreless multimode) structure is likely one of the simplest to design compared to other structures, providing a significant advantage [10]. To stimulate the evanescent wave that causes SPR resonance in the metal film, most fiber optic SPR sensors require cladding removal through methods such as chemical dissolution [11,12]. The no-core fiber (NCF) is a specialized type of fiber that lacks a central core, consisting only of cladding and coating. This unique design enables the cladding surface to function as a sensing interface, offering distinctive transmission characteristics. With a uniform RI throughout, the fiber itself serves as the core while the surrounding medium acts as the cladding, forming a double-layer circular waveguide structure [13]. Due to the unique structure of coreless fibers, the sensor exhibits heightened sensitivity towards changes in environmental parameters. The concentration of analytes can be indirectly measured by monitoring alterations in the wavelength of surface plasmon resonance absorption peaks.

After measuring the parameters and collecting the optical signal with an optical fiber sensor, demodulation of the signal is necessary. In terms of spectra, parameter measurement typically involves observing wavelength drift and intensity changes, necessitating accurate detection of spectral drift and intensity changes in wavelength or frequency to achieve high accuracy [13]. Therefore, high-resolution detection hardware is required. In recent years, the advancement of artificial intelligence technology has been astonishing. Recent spectral modeling has demonstrated the potential of convolutional

This work was supported by the National Natural Science Foundation of China (NSFC) (62365013 and 62175097), the Key projects of Jiangxi Provincial Natural Science Foundation (20242BAB26021), the Jiangxi Provincial Natural Science Foundation (20242BAB20064), the European Union's MSCA-DN project no.101119624 OWIN6G and Royal Society International Exchanges 2022 (IES\R1\221008). (Corresponding authors: Hong Yang, Bin Liu, Qiang Wu)

Xiao-xiao Liao, Hong Yang, Juan Liu, Yingying Hu, Yue Zhang, Wei-qing Liu, Fu Yue, Qiang Wu and Bin Liu are with Key Laboratory for Optoelectronic Information Perception and Instrumentation of Jiangxi Province, Nanchang Hangkong University, Nanchang 330063, China (e-mail: yanghong@nchu.edu.cn; liubin@nchu.edu.cn). Qiang Wu is also with Faculty of Engineering and Environment, Northumbria University, Newcastle Upon Tyne NE1 8ST, UK. (e-mail: qiang.wu@northumbria.ac.uk) Andrew R Pike is with Department of Chemistry, School of Natural and Environmental Sciences, Newcastle University, Newcastle Upon Tyne NE1 7RU, UK.

neural networks (CNNs) to surpass traditional statistical and machine learning models. CNNs are a subset of deep learning that have achieved remarkable success in various domains such as image classification [14], video analysis [15], and drug discovery [16]. AI-based optimization algorithms have great advantages and allow us to obtain more reliable analysis of data, particularly when dealing with a wide range of input parameters. Furthermore, these algorithms enable us to comprehend correlations between parameters across the entire parameter range simultaneously, simplifying the optimization process for complex structures [17]. Moreover, compared to traditional demodulation methods, CNNs exhibit higher accuracy and superior generalization capabilities in recognizing and predicting complex optical signals with large volumes of data due to their autonomous learning characteristics [18-20]. This paper introduces a CNN model designed to demodulate the spectral signal of an SPR fiber sensor and predict the RI.

II. EXPERIMENTAL SYSTEM AND ALGORITHM

A. Experimental system

At the initial stage of the experiment, we encountered a decision regarding the structural design of the optical fiber. Only by identifying an optimal fiber structure that both facilitates enhanced light leakage and stimulates a more pronounced SPR effect were we able to achieve heightened RI sensitivity. Subsequently, we fabricated a fiber SPR sensor for subsequent RI prediction analysis based on neural network algorithms. As depicted in Fig.1, our proposed sensor features a heterogeneous core fiber (M-N-M) configuration comprising two identical multimode fibers (MMF) with 62.5μm cores and 125μm cladding diameters fused at both ends of a 2cm length of no-core fiber (NCF) with a 125μm core diameter, while utilizing the surrounding medium as cladding material. The optical fiber is gently cleansed using anhydrous ethanol followed by the removal of any residual dust particles with distilled water. To optimize performance and determine the ideal coating thickness for maximum sensitivity of RI, a 40 nm gold film was deposited onto the optical fiber sensor using high-temperature evaporation, which is a commonly employed technique for preparing gold films. Figure 2 shows the scanning electron microscope (SEM) image of the optical fiber end face after gold film deposition. The fiber optic sensor can be employed for measuring the external RI by applying a thin metallic coating.

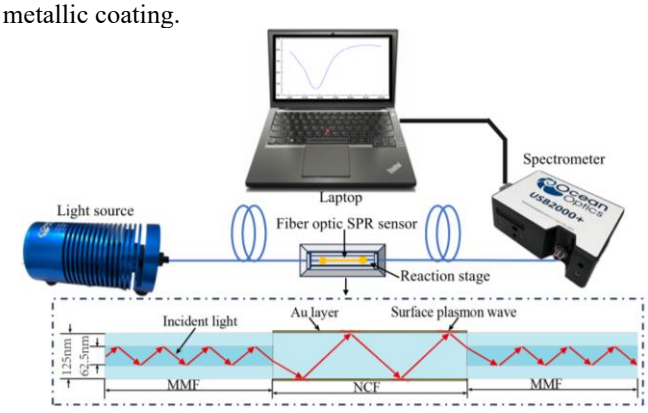

Fig.1. Schematic diagram of the experimental setup and the overall MNM structure of the optical fiber sensor.

Next, a sensing system was designed for the proposed biosensor, shown in Fig.1, which includes a wideband light source (HL-2000, Ocean Optics), a spectrometer (USB2000+, Ocean Optics), a computer, and a fiber SPR biosensor. To connect the light source, sensor, and spectrometer, MMF transmission fiber is used. The incident light first travels from the MMF to the NCF through the fiber core. The incident light enters the gold film in the form of an evanescent field, and strong light absorption occurs when the parallel component of the incident light wave vector matches the parallel component of the surface plasmon wave. The output spectrum signal appears at a specific wavelength of SPR drop, called the resonance wavelength [21]. When the external RI changes, the SPR inclination will shift accordingly. The collected signal can be displayed and monitored by a computer connected to the spectrometer.

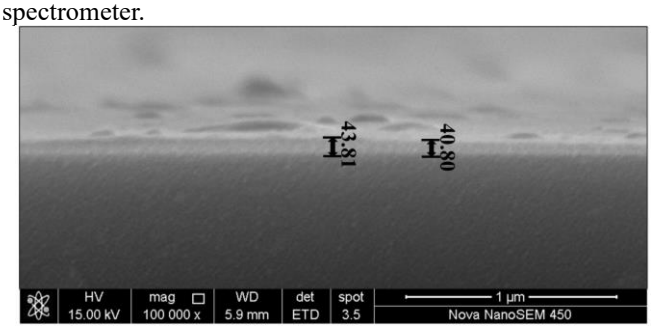

Fig.2.Optical fiber end imaged by scanning electron microscopy showing the thickness of gold film deposited on the surface of the optical fiber sensor.

B. Convolutional network structure and output evaluation parameters

The composition of CNNs typically consists of three types of layers (or building blocks): convolutional layers, pooled layers, and fully connected layers. The convolution layer is utilized for feature extraction, while the pooling layer serves to reduce both the dimension of features and the number of parameters. Subsequently, the fully connected layer is employed to map these extracted features onto the output space. Spectral data is commonly represented as a sequence of wavelength intensity values. Prior to being fed into a CNN, it is necessary to convert spectral data into an appropriate format that represents the data in matrix form [22]. Convolutional layer: Different from ordinary neural networks, CNN has a weight-sharing convolutional layer structure. If we let H_l be the input feature map of the convolution layer, H_0 is the original feature graph, S is the result of the convolution operation, H_{l+1} is the output feature graph of the convolution layer, K is the convolution kernel, i is the index of the feature graph, p is the index on the convolution kernel, b is the offset, and $f(x)$ is the activation function. Therefore, the one-dimensional convolution operation can be expressed as:

$$S(i) = \sum_p H_l(i+p)K(p)$$
$$H_{l+1} = f(S+b) \quad (1)$$

One-dimensional pooling layer: The pooling layer is also known as the down sampling layer, which is used to reduce and extract effective features. The pooling layer is divided into the maximum pooling layer and the average pooling layer. Let layer l be the pooling layer, k be the size of the pooling window,

and p be the index of the pooling window. Therefore, the formulas for maximum pooling and mean pooling can be expressed as:

$$H_{l+1}(i) = \max_{p \in k} H_l(i+p)$$
$$H_{l+1}(i) = \frac{1}{k}\sum_p H_l(i+p) \quad (2)$$

Activation function: The activation function is used after the convolutional layer, which can carry out nonlinear transformations of the output of the convolutional layer and enhance the expression ability of the neural network. Common activation functions include the sigmoid function, ReLU function, tanh function, and so on. The activation functions used here are:

$$ReLU(x) = \begin{cases} 0, & if\ x \le 0, \\ x, & if\ x > 0. \end{cases} \quad (3)$$

When the eigenvalue is less than or equal to zero, the output is zero, and when it is greater than zero, the output is equal to the input eigenvalue.

Evaluation metrics for CNNs are often used to measure a model's performance in classification or regression tasks. Common evaluation indexes of neural network models include the decision coefficient R^2, the mean square error (MSE), the mean absolute error (MAE), and the root mean square error (RMSE) [23].

C. Construct convolutional neural network to predict the refractive index

The neural network structure built in the experiment is shown in Fig. 3. Firstly, in order to improve the training efficiency and ensure the stability of the model, we first input the spectral data into the model after normalization. Then eight convolution layers are used to extract features from the data, and three pooling layers are used to reduce the sampling dimension and compress features. One Flatten layer is used to reduce the output data dimension to one dimension. The output layer outputs the predicted RI information. Transfer learning method and Adam optimizer are used to train the model to improve the performance and efficiency of the model. Through this algorithm, the direct mapping of the spectrum to RI can be realized. The normalization formula can be expressed as:

$$X_{nor} = \frac{x - x_{min}}{x_{max} - x_{min}} \quad (4)$$

The variable X represents one-dimensional spectral data, indicating the intensity of light, while x_{min} and x_{max} represent the minimum and maximum values of light intensity. After normalization, the obtained value falls within the range of (0,1). To preserve boundary information without any loss, considering that non-zero boundary values exist in the selected spectral range, each convolutional layer employs zero-padding when processing input data. This ensures the integrity of the boundary data across all layers. Subsequently, the normalized data is fed into eight convolutional layers with a kernel size of 3 each. Additionally, adjacent convolutional layers are connected to pooled layers for extracting important features. In this process, Max pooling is used to output the maximum value of each area block, thereby reducing the number of features, improving the calculation speed, and preventing overfitting. Finally, the output data is vectorized through the Flatten layer and then passes through the Dense layer to finally get the prediction result.

Transfer learning presents a variety of applications, among which the use of pre-trained models is particularly common. Pre-trained models are trained on large data sets and are often used to solve specific tasks. In the early stages of model training, its weights are generated randomly, which leads to the possibility of differences in the results of each training. In order to improve the accuracy of the model and reduce the calculation time, an effective method is to save the weight value of the best pre-trained model. At each subsequent training session, we can re-train with these saved best weights. This not only accelerates the convergence rate of the model but also helps to improve the prediction accuracy of the model.

In this work, the adaptive moment estimator (Adam) is used to optimize the learning rate, which is a commonly used gradient descent optimization method. The Adam optimizer combines the ideas of Momentum and adaptive learning rate adjustment. This helps to accelerate convergence during optimization, especially for loss function surfaces with longer, flatter valley shapes, by leveraging historical gradient information to accumulate "velocity" that allows parameter updates to occur more quickly in the relevant direction [24]. Compared with traditional optimization algorithms such as Stochastic Gradient Descent (SGD), Adam combines momentum and adaptive learning rate, which can converge more quickly toward the general area of the optimal solution in most cases. It can automatically adjust the learning rate of

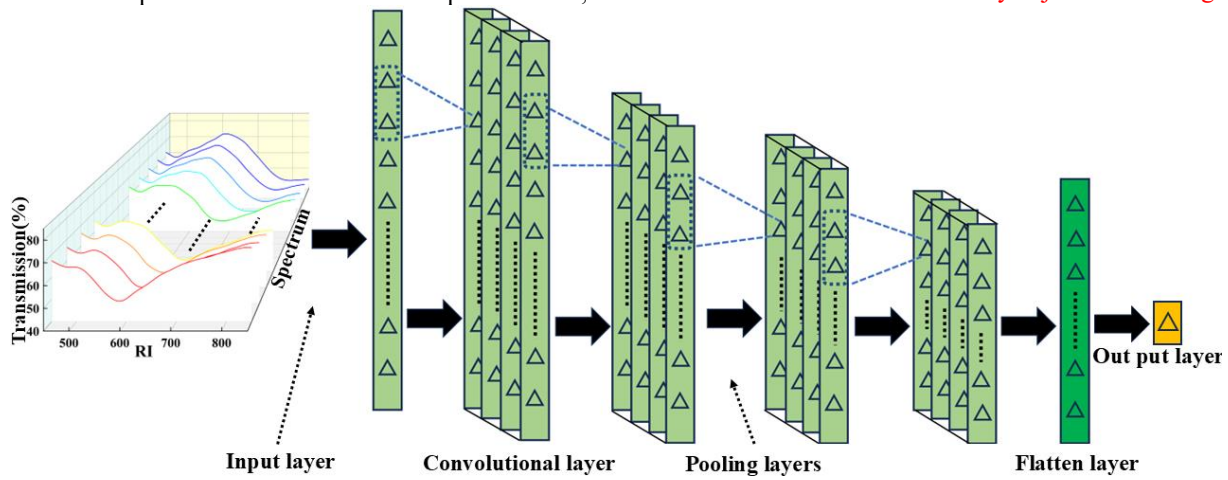

Fig. 3. The neural network structure shows one input layer, eight convolutional layers, three pooling layers, one Flatten layer, and an output layer.

each parameter, so that each parameter can be updated at its own pace, especially for complex neural networks, which can effectively reduce the training time. In the training process, MSE is used as the loss function, R^2 is used as the main evaluation standard, and they are both calculated from the predicted value and the real value. The closer R^2 is to 1, the more accurate the output is. During the training process, a self--stop program was set, and when R^2 did not grow after 30 training cycles, the model would automatically stop the training and save the parameters. All code is written in Python and calls the keras library.

III. Experimental Results and Analysis

A. Spectral data acquisition

When the structure and geometry of the multimode fiber optic SPR sensor are fixed, the thickness of the metal film supporting the SPR plays a crucial role in determining the performance of the SPR sensor [25]. The RI sensitivity of the fiber optic SPR sensor with a gold film thickness of 40 nm was evaluated. The sensing region of the optical fiber probe is immersed in solutions with varying refractive indices to induce corresponding changes in resonance inclination angle. Figure 4 illustrates variations in normalized transmission spectra for this sensor based on surrounding solutions of different refractive indices (1.332 ~ 1.435). It can be observed that as the RI increases, there is a shallowing and broadening effect on the SPR valley while simultaneously shifting towards longer wavelengths.

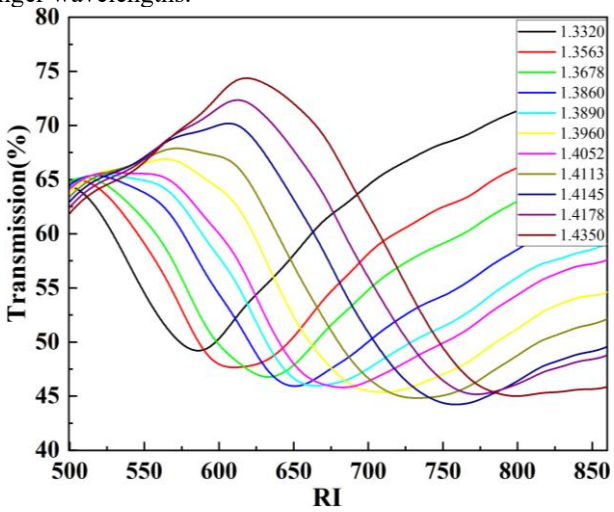

Fig.4. Spectral changes in liquids with different refractive indices.

After collecting the spectra of different refractive indices, 1D-CNN is used to extract and predict the features of the data. Figure 5 shows the RI prediction flowchart. Firstly, the training set data was input into 1D-CNN for training to obtain the model. In the training process, transfer learning was introduced to optimize the model to improve the prediction accuracy. Finally, the trained model is used to predict the prediction set and obtain the RI.

Based on the sensor with a film thickness of 45 nm, a total of 210 spectral data were collected in this experiment. Each spectrum consisted of 1,783 sampling points, with the measurement bandwidth ranging from 400 to 1,000nm and the RI ranging from 1.3320 to 1.4350. The model's performance is evaluated using MSE and R^2 indicators, which measure how closely the predictions align with the observations. To assess the model's accuracy, we evenly divided the dataset into ten groups, where nine groups were used for training and one group remained untrained for testing purposes. The SPR spectral data was then inputted into CNN for predicting the RI.

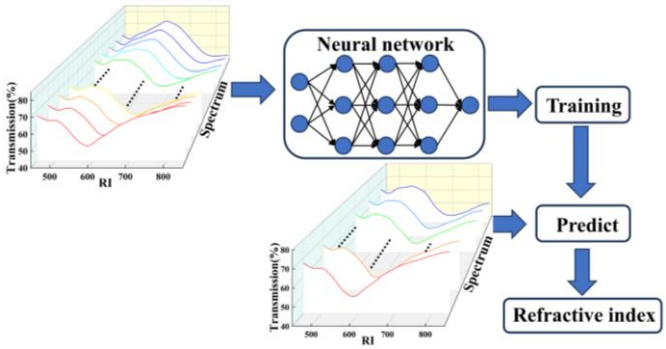

Fig. 5. Refractive index prediction flow chart.

B. Analysis of the refractive index prediction results

The change curve of the MSE loss function in the training set and test set is presented in Fig. 6 (a), with the number of iterations plotted on the abscissa. From Fig. 6 it can be observed that the loss function curve gradually converges to zero, indicating an improvement in RI prediction with increasing iterations. In Fig.6 (b), a scatter plot of predicted RI values is shown, where the true value of RI is represented on the abscissa and the predicted value on the ordinate axis. The proximity of scatter points to the $Y=X$ line signifies a closer match between true and predicted RI values while achieving an output accuracy (R^2) of 0.98676. These results demonstrate that our CNN model effectively extracts relevant features from SPR spectrum data and enables direct mapping to RI.

Figure 6 (c) shows the relationship between the resonant wavelength of the sensor and the real measured value RI, and Figure 6 (d) shows the relationship between the resonant wavelength of the sensor and the output predicted value RI of the CNN algorithm. It can be seen from the two figures that the resonant wavelength of the sensor increases nonlinearly with the increase of RI, which can be well fitted with the reciprocal function [26], which means that the sensitivity also increases nonlinearly with the increase in RI. For SPR sensors, sensitivity is defined as the ratio of the change in resonance wavelength $\Delta\lambda$ to the change in surrounding refractive index dn. Since the experimental data can be fitted well with the reciprocal function, the sensitivity of the sensor can be calculated by taking the derivative of the fitting function. Therefore, the sensitivity of the above SPR sensor can be calculated as follows:

$$S_1 = \frac{\mathrm{d}\Delta\lambda}{\mathrm{dn}} = \frac{d\left(168+\frac{114}{1.6136-X}\right)}{dn} = \frac{114}{(1.6136-X)^2} \quad (9)$$

$$S_2 = \frac{\mathrm{d}\Delta\lambda}{\mathrm{dn}} = \frac{d\left(267+\frac{73}{1.5694-X}\right)}{dn} = \frac{73}{(1.5694-X)^2} \quad (10)$$

The results are depicted in Fig.7 across the RI range of 1.332 to 1.435. The measured RI sensitivity of the SPR sensor exhibits nonlinear growth between 1437.6 and 3573.8nm/RIU, while the predicted RI sensitivity shows nonlinear growth between 1295.2 and 4041.3nm/RIU. A comparison between the predicted RI output from the convolutional neural network

and the actual measured RI reveals that the predicted output demonstrates a superior degree of non-linear fitting, with an R^2 value reaching 0.98383. Sensors based on optical fiber SPR are currently receiving the greatest research interest, mainly due to their extremely high RI sensitivity, reaching thousands of nm/RIU. We compared the performance of our proposed sensor with that of existing sensors, as shown in Table 1. It can be seen that the emergence of new fiber structures such as photonic crystal fibers has greatly improved the sensitivity and detection capability of fiber SPR sensors, but these fibers are usually expensive. Although not as sensitive as photonic crystals or other novel sensor structures, our sensor has the advantages of a simple manufacturing process and high cost-effectiveness compared to these sensors.

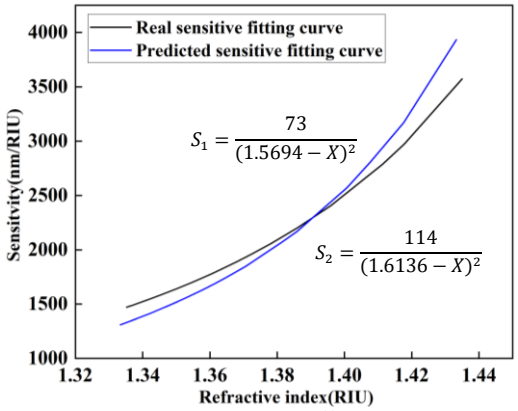

Fig. 7. Sensitivities at different RI.

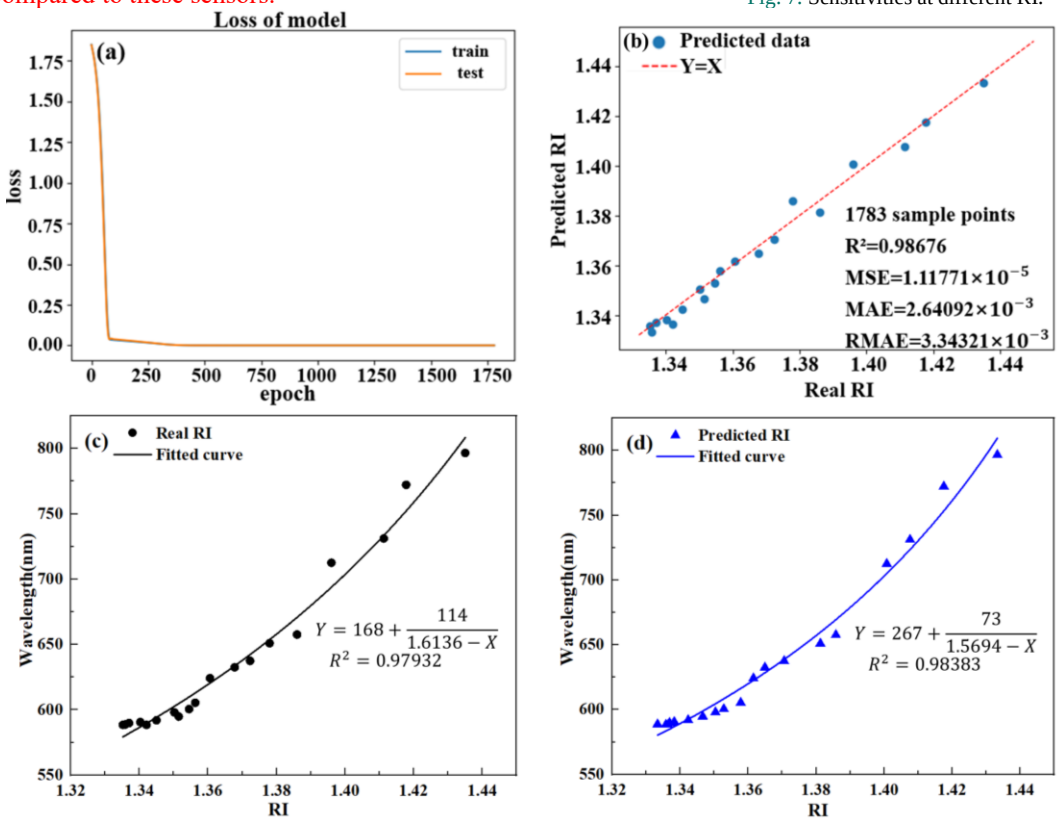

Fig 6. (a) Trends in loss curves during training and (b) scatter plot of RI value prediction. (c) Actual RI fitting results and (d) predicted RI fitting results.

TABLE I
COMPARISON OF VARIOUS INTENSITY-MODULATED RI SENSORS.

Sensors	RI sensitivity (nm/RIU)	Measurement range
Tapered fiber-optical sensor [27]	Max.1500	1.333~1.338
Bare-core optical-fiber sensor [28]	Max.3610.4	1.333~1.353
Tilted fiber Bragg gratings [29]	Max.510	1.335~1.432
Asymmetric double-core double-D-type PCF-SPR sensor [30]	Max.21000	1.33~1.42
Wedged fiber optic (SPR) sensor [31]	Max.8161	1.333-1.404
MNM sensor (this work)	Max.4041.3	1.332~1.435

C. Optimize the resolution requirements of sensor signals

In traditional methods, the shifts in angle and wavelength and any variations in SPR spectra are often difficult to observe, requiring high sensitivity of the spectrometer, which significantly increases the cost of the spectrometer. We propose a method based on CNNs to predict the RI by sampling the spectral data at intervals. Experimental results show that this method can significantly reduce the cost of the required spectrometer.

Figure 8 shows the sampling process of the spectrum. The original sampling number of the spectrum was 1,783, and samples were taken every 2, 3, 6, 12, and 23 points on average. The sampling process is shown in Fig.8, where (a) samples every point and (b) every other point to obtain 891 sampling points. The spectrum from sampling 891 points is shown in Fig.9 (a). In a similar fashion the spectra from 594, 279, and 149 sampling points, are shown in Fig.9 (b), (c), and (d) respectively. All the data sets are divided into 10 groups, nine of them are trained, and the model is tested with the remaining set of untrained data and cross-verified 10 times.

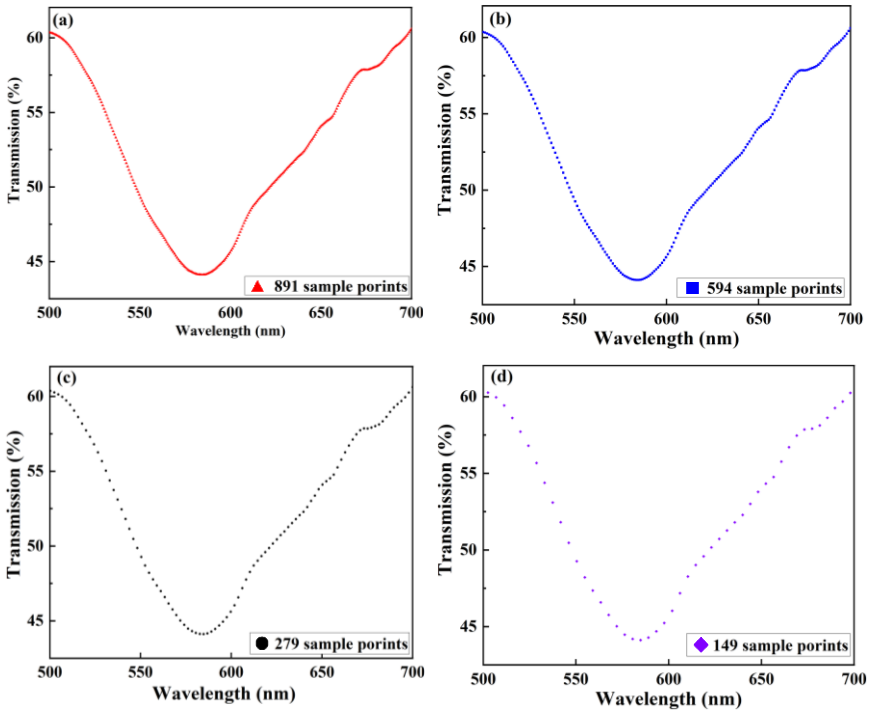

Fig.9. The spectra at points (a) 891, (b) 594, (c) 279 and (d) 149 were sampled.

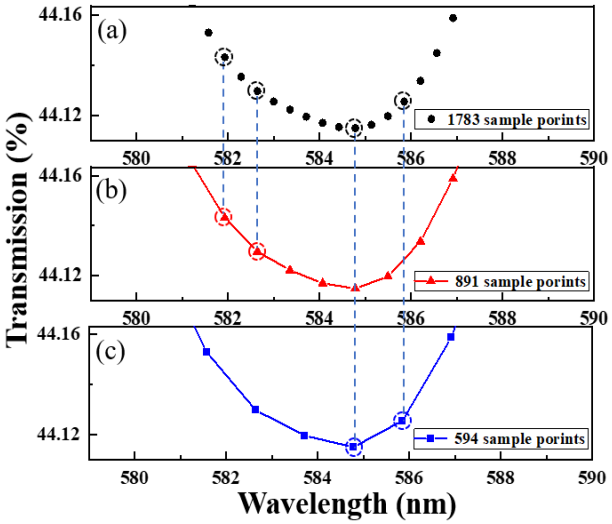

Fig.8. (a)-(c) Resampling procedure, (a)-(c) 1783, 891 and 594 sample points

The results of RI predictions for different sampling points are illustrated in Fig.10 (a-e). The R^2 values for the sampling points-1,783, 891, 594, 149, and 78 are determined as 0.98739, 0.98403, 0.98624, 0.98358, and 0.90043 respectively. Fig.10 (f) presents a boxplot depicting the accuracy R^2 at various sampling points with the horizontal axis representing the number of sampling points and the vertical axis indicating the predicted R^2 value. Observations reveal that the accuracy of sampling points ranging from 1,783 to 149 exceeds a threshold of over 98%, while it drops to an R^2 value of only 0.90043 when considering a smaller number of sampling points such as 78. Table 1 provides an overview of the evaluation indexes corresponding to different numbers of sampling points. The average accuracy R2 values for each respective number of sampling points 1,783, 891, 594, 149, and 78 were calculated as 0.987472, 0.987533, 0.98598, 0.983549, and 0.930094 respectively. The findings depicted in Fig.9 and Table II demonstrate that reducing the number of sampling points to 149 has minimal impact on RI prediction accuracy. Therefore, the resolution requirement for OSA need not be excessively high and so cost-effective OSA devices can be utilized for measurement purposes.

TABLE II
INDEX OF REFRACTIVE INDEX OF DIFFERENT SAMPLING POINTS

Sampling number	1738	891	594	149	78
Average R^2	0.987	0.987	0.989	0.983	0.930
Average MS (10^{-6})	9.038	10.224	8.510	13.326	56.893
Average MAE (10^{-3})	2.149	2.393	2.023	2.641	5.639
Average RMSE (10^{-3})	3.179	3.172	2.873	3.619	7.286

IV. CONCLUSION

In this paper, a new kind of 1D-CNN algorithm demodulated optical fiber SPR sensor for RI sensing was proposed and investigated. The structure of the SPR fiber sensor was based on a multimode-coreless multimode design, and spectral data from different RI environments were collected and grouped. Finally, the 1D-CNN algorithm was used to predict the RI sensitivity and the accuracy was greater than 98%. The sensor has a high RI sensitivity over a wide range of values, 1.3330-1.4102. The maximum sensitivity is 4041.3nm/RIU, and the prediction accuracy is higher than 98% at low resolution. The experiment proves that the 1D-CNN algorithm can be used for spectral demodulation of an optical fiber SPR sensor, and also proves that the method can reduce the need for costly detection systems. We expect that this approach can be widely used in chemical and biological fields to measure RI, or other measurements that can induce RI changes, such as concentration or synthesis changes in chemical reactions.

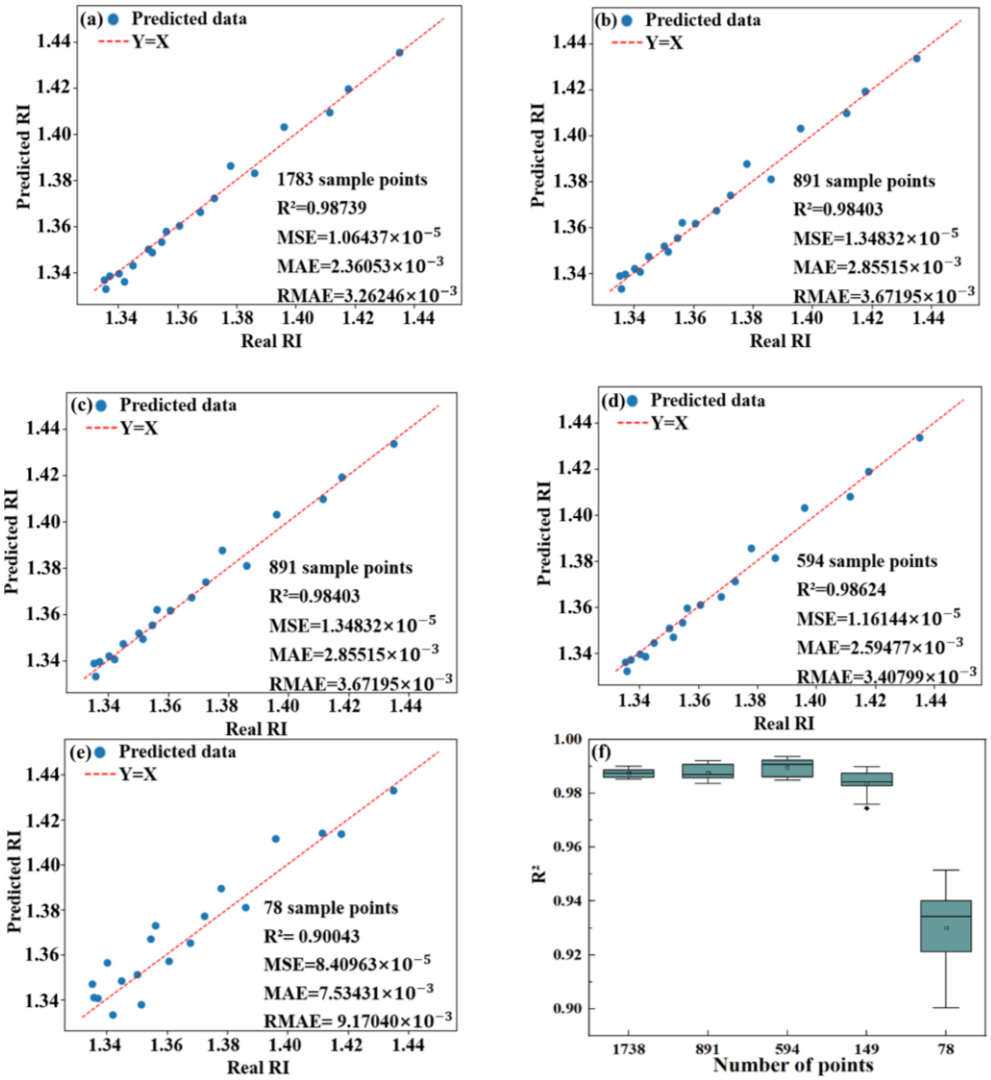

Fig.10. Prediction results for sampling points (a)1783, (b)891, (c) 594, (d) 149, and (e) 78. (f) Box plot of refractive index at different sampling points.

V. REFERENCES

[1] J. Zhang, X. Mai, X. Hong, Y. Chen, and X. Li, "Optical fiber SPR biosensor with a solid-phase enzymatic reaction device for glucose detection," Sens. Actuators B, vol. 366, p. 131984, Sep. 2022.

[2] Y. Zhao, Q. Wu, and Y. Zhang, "Simultaneous measurement of salinity, temperature and pressure in seawater using optical fiber SPR sensor," Measurement, vol. 148, p. 106792, Dec. 2019.

[3] T. Iqbal, Sanjeev Kumar Raghuwanshi, and S. Kumar, "Recent Advancement in Fiber-Optic-Based SPR Biosensor for Food Adulteration Detection—A Review," IEEE T. Nanobiosci., vol. 22, no. 4, pp. 978–988, Oct. 2023.

[4] Z. Wang, Ragini Raj Singh, C. Marques, W. Huang, B. Zhang, and S. Kumar, "Taper-in-taper fiber structure-based LSPR sensor for alanine aminotransferase detection," Opt. Express, vol. 29, no. 26, pp. 43793–43793, Dec. 2021.

[5] R. C. Jorgenson and S. S. Yee, "A fiber-optic chemical sensor based on surface plasmon resonance," Sens. Actuators B, vol. 12, pp. 213-220, 1993.

[6] W. Yang, J. Gao, Z. Li, C. Li, Y. Cheng, Y. Huo, S. Jiang, and M. Jiang, "High performance D-type plastic fiber SPR sensor based on a hyperbolic metamaterial composed of Ag/MgF_2," J. Mater. Chem. C, vol. 9, no. 39, pp. 13647–13658, Jan. 2021.

[7] C. Liu, P. Wu, C. Shi, C. Liu, Y. Wei, L. Hu, R. Wang, and T. Jiang, "Fiber SPR micro displacement sensor based on heterocore structure of graded index multimode fiber," Opt. Commun., vol. 529, p. 129095, Feb. 2023.

[8] C. Liu. P. Wu, Y. Wei, B. Li, Y. Su, X. Zhao, R. Wang, and L. Li, "Dual-detection-parameter SPR sensor based on graded index multimode fiber," Sens. Actuators A, vol. 335, pp. 113360–113360, Mar. 2022.

[9] C. Tang, D. Yang, T. Cheng, and S. Yang, "Bidirectional Design for SPR-Photonic Crystal Fiber Magnetic Field Sensor Based on Deep Learning," IEEE Sens. J., vol. 24, no. 3, pp. 4091–4101, Feb. 2024.

[10] N. S. Fabian, A. B. Socorro-Leranoz, I. D. Villar, S. Diaz, and I. R. Matias, "Multimode-Coreless-Multimode Fiber-Based Sensors: Theoretical and Experimental Study," J. Lightwave Technol., vol. 37, no. 15, pp. 3844–3850, Aug. 2019.

[11] L. Coelho, M. de, J. L. Santos, S. Ferreira, P. S. André, and D. Viegas, "Sensing Structure Based on Surface Plasmon Resonance in Chemically Etched Single Mode Optical Fibres," Plasmonics, vol. 10, no. 2, pp. 319–327, Nov. 2014.

[12] N. A. M. Zainuddin, M. M. Ariannejad, P. T. Arasu, S. W. Harun, and R. Zakaria, "Investigation of cladding thicknesses on silver SPR based side-polished optical fiber refractive-index sensor," Results Phys., vol. 13, p. 102255, Jun. 2019.

[13] Y. Zhao, J. Zhao, and Q. Zhao, "Review of no-core optical fiber sensor and applications," Sens. Actuators A, vol. 313, p. 112160, Oct. 2020.

[14] P. Zhang, Y. Wang, Y. Chen, X. Lei, Y. Qi, J. Feng, and X. Liu, "A High-Speed Demodulation Technology of Fiber Optic Extrinsic Fabry-Perot Interferometric Sensor Based on Coarse Spectrum," Sensors, vol. 21, no. 19, pp. 6609–6609, Oct. 2021.

[15] Y. Park and H.-S. Yang, "Convolutional neural network based on an extreme learning machine for image classification," Neurocomputing, vol. 339, pp. 66–76, Apr. 2019.

[16] D. Kitaguchi, N. Takeshita, H. Matsuzaki, T. Igaki, H. Hasegawa, and M. Ito, "Development and Validation of a 3-Dimensional Convolutional Neural Network for Automatic Surgical Skill Assessment Based on Spatiotemporal Video Analysis," JAMA Netw. Open, vol. 4, no. 8, p. e2120786, Aug. 2021.
[17] Z. Shen and R. A. Viscarra Rossel, "Automated spectroscopic modelling with optimised convolutional neural networks," Sci. Rep., vol. 11, no. 1, Jan. 2021.
[18] Z. Zhang et al., "An improved phase generated carrier demodulation algorithm with high stability and low harmonic distortion," Optics Communications, vol. 524, pp. 128800–128800, Jul. 2022.
[19] R. Yamashita, M. Nishio, R. K. G. Do, and K. Togashi, "Convolutional Neural networks: an Overview and Application in Radiology," Insights Imaging, vol. 9, no. 4, pp. 611–629, Jun. 2018.
[20] X. Li, Y. Wu, C. Tang, Y. Fu, and L. Zhang, "Improving generalization of convolutional neural network through contrastive augmentation," Knowl-Based Syst., vol. 272, pp. 110543–110543, Jul. 2023.
[21] J. S. Velázquez-González, D. Monzón-Hernández, F. Martínez-Piñón, and I. Hernández-Romano, "Highly Sensitive Surface Plasmon Resonance-based Optical Fiber Multi-parameter Sensor," Procedia Engineering, vol. 168, pp. 1249–1252, 2016.
[22] K. Shen and D. Zhao, "Fault Diagnosis for Aircraft Hydraulic Systems via One-Dimensional Multichannel Convolution Neural Network," Actuators, vol. 11, no. 7, p. 182, Jul. 2022.
[23] K. Mei, J. Liu, X. Zhang, Nandana Rajatheva, and J. Wei, "Performance Analysis on Machine Learning-Based Channel Estimation," IEEE Transactions on Communications, vol. 69, no. 8, pp. 5183–5193, May 2021.
[24] A. H. Khan, X. Cao, S. Li, V. N. Katsikis, and L. Liao, "BAS-ADAM: an ADAM based approach to improve the performance of beetle antennae search optimizer," *IEEE/CAA Journal of Automatica Sinica*, vol. 7, no. 2, pp. 461–471, Mar. 2020.
[25] H. Suzuki, M. Sugimoto, Y. Matsui, and Jun Kondoh, "Effects of gold film thickness on spectrum profile and sensitivity of a multimode-optical-fiber SPR sensor," Sens. Actuators B, vol. 132, no. 1, pp. 26–33, May 2008.
[26] Q. Han, X. Lan, J. Huang, A, Kaur, T. Wei, Z. Gao, and H. Xiao, "Long-Period Grating Inscribed on Concatenated Double-Clad and Single-Clad Fiber for Simultaneous Measurement of Temperature and Refractive Index," IEEE Photonic. Tech. L., vol. 24, no. 13, pp. 1130–1132, Jul. 2012.
[27] J. Miller *et al.*, "Biconically Tapered Fiber Optic Probes for Rapid Label-Free Immunoassays," *Biosensors*, vol. 5, no. 2, pp. 158–171, Apr. 2015.
[28] T. K. Yadav, R. Narayanaswamy, M. H. Abu Bakar, Y. M. Kamil, and M. A. Mahdi, "Single mode tapered fiber-optic interferometer based refractive index sensor and its application to protein sensing," *Optics Express*, vol. 22, no. 19, p. 22802, Sep. 2014.
[29] M. D. Baiad et al., "Surface plasmon resonance sensor interrogation with a double-clad fiber coupler and cladding modes excited by a tilted fiber Bragg grating," Optics Letters, vol. 38, no. 22, p. 4911, Nov. 2013.
[30] Z. Zhang *et al.*, "Dual-Core Photonic Crystal Fiber Surface Plasmon Resonance Sensor with High Sensitivity and Narrow FWHM," *Plasmonics*, vol. 19, no. 1, pp. 495–504, Aug. 2023.
[31] L. Li et al., "Wedged Fiber Optic Surface Plasmon Resonance Sensor for High-Sensitivity Refractive Index and Temperature Measurements," Sensors, vol. 22, no. 23, pp. 9099–9099, Nov. 2022.

Xiao-Xiao Liao received the B.S. degree from Nanchang Hangkong University, Nanchang, China, in 2022. He is currently pursuing the M.S. degree in electronic information engineering with Nanchang Hangkong University, Nanchang, China. His research interests focus on optical fiber sensors.

Hong Yang received the B.S. and Ph.D. degrees from Nanchang University, China. He is a lecturer with the Key Laboratory of Opto-Electronic Information Science and Technology of Jiangxi Province, Nanchang Hangkong University, China. His current research interests include optical smart metal structure and optical fiber sensing.

Qiang Wu received the B.S. and Ph.D. degrees from Beijing Normal University and Beijing University of Posts and Telecommunications, Beijing, China, in 1996 and 2004, respectively. From 2004 to 2006, he worked as a Senior Research Associate in City University of Hong Kong. From 2006 to 2008, he took up a research associate post in Heriot-Watt University, Edinburgh, U.K. From 2008 to 2014, he worked as a Stokes Lecturer at Photonics Research Centre, Dublin Institute of Technology, Ireland. He is an Associate Professor / Reader with Faculty of Engineering and Environment, Northumbria University, Newcastle Upon Tyne, United Kingdom. His research interests include optical fiber interferometers for novel fiber optical couplers and sensors, nanofiber, microsphere sensors for bio-chemical sensing, the design and fabrication of fiber Bragg grating devices and their applications for sensing, nonlinear fiber optics, surface plasmon resonant and surface acoustic wave sensors. He has over 280 publications in the area of photonics and holds 8 invention patents. He is an Editorial Board Member of Scientific Reports, an Associate Editor for IEEE Sensors Journal, and an Academic Editor for Journal of Sensors.

Juan Liu received her Ph.D. degree from Beijing Normal University, China. She is a lecturer with Key Laboratory of Nondestructive Test (Ministry of Education) of Nanchang Hangkong University, China. Her main research interest is fiber optic sensing.

Yingying Hu received her Ph.D. degree from University of Science and Technology of China, China. She is a lecturer with Key Laboratory of Nondestructive Test (Ministry of Education) of Nanchang Hangkong University, China. Her main research interests are fiber optic sensing and quantum random number.

Yue Zhang received her Ph.D. degree from Central South University, China. She is a lecturer with Key Laboratory of Opto-Electronic Information Science and Technology of Jiangxi Province, Nanchang Hangkong University, China. Her current research interests include functional materials and flexible pressure sensors.

Wei-qing Liu is a professor at the Nanchang Hangkong University in China. He received his PhD degree from the Hefei Institutes of Physical Science, Chinese Academy of Sciences in 2010. His research interests focus on energy storage, sensors, solar cells, and photoelectrochemical devices.

Yue Fu is a lecturer with the Key Laboratory of Opto-Electronic Information Science and Technology of Jiangxi Province, Nanchang Hangkong University, China. Her current research interests include ultrasonic detection and photoelectric detection.

Andrew R. Pike received a B.Sc. degree in Medicinal Chemistry from Newcastle University, U.K., a M.Sc. degree in functional molecular chemistry from Hokkaido University, Japan, and his Ph.D. in DNA-silicon hybrid sensing materials 2001 back at Newcastle University. He spent three years as a Postdoctoral Research Assistant working on DNA-inspired nanomaterials before joining INEX Ltd. to develop rapid biothreat sensing systems. He returned to academia as a RCUK Academic Fellow, in 2005. and has since been a Lecturer and a Senior Lecturer in chemical nanoscience at Newcastle University. He is now Director of Chemistry within the School of Natural and Environmental Sciences and CTO of NunaBio Ltd. His research focuses on nanomaterials for application in sensor systems.

Bin Liu received the B.S. and Ph.D. degrees from Sun Yat-sen University, China. Dr. Liu is a Professor with the Key Laboratory of Opto-Electronic Information Science and Technology of Jiangxi Province, Nanchang Hangkong University, China. He has over 100 publications in the area of photonics and holds 10 invention patents. His current research interests include optical fiber interferometer and the application for sensing, fiber bio-chemical sensors, optical micro-cavity and the application for sensing, surface plasmon resonant, Design and application of micro-nano photonic devices, optical nonlinearity and optical soliton, FBG sensing and distributed fiber sensing.